Charge Injection and Electrical Response in Low-Temperature SnO 2 -Based Efficient Perovskite Solar Cells

Maria Ulfa, Pengjiu Wang, Jie Zhang, Jiawen Liu, Willy Daney de Marcillac, Laurent Coolen, Sebastien Peralta, Thierry Pauporte

Please cite this paper as : M. Ulfa, P. Wang, J. Zhang, J. Liu, W. Daney de Marcillac, L. Coolen, S. Peralta, T. Pauporté, Charge Injection and Electrical Response in Low Temperature SnO2-Based Efficient Perovskite Solar Cells. ACS Appl. Mater. Interfaces, 10 (2018) 35118–35128.

Charge Injection and Electrical Response in Low Temperature SnO_2-Based Efficient Perovskite Solar Cells

Maria Ulfa,[a] Pengjiu Wang,[a] Jie Zhang,[b] Jiawen Liu,[c] Willy Daney de Marcillac[c] Laurent Coolen,[c] Sébastien Peralta,[d] Thierry Pauporté*[a]

[a] Chimie ParisTech, PSL Research University, CNRS, Institut de Recherche de Chimie Paris (IRCP), 11 rue P. et M. Curie, F-75005 Paris, France.

[b] School of Chemistry and Chemical Engineering, South China University of Technology, Guangzhou, Guangdong, China

[c] Sorbonne Université, CNRS, Institut de NanoSciences de Paris, INSP, F-75005 Paris, France.

[d] Laboratoire de Physico-chimie des Polymères et Interfaces (LPPI), Université de Cergy-Pontoise, 5 mail Gay-Lussac. 95031 Cergy-Pontoise, France.

* Author for correspondence: thierry.pauporte@chimie-paristech.fr

Abstract

Defining low-temperature engineering protocols for efficient planar perovskite solar cells (PSCs) preparation is important for fabrication simplification and low-cost production. In the present work, we have defined a low-temperature (123°C) protocol for the preparation from a solution of SnO_2 layers which are efficient for an application as electron transporting layer (ETL) in PSCs. Thin, conformal and transparent layers have been obtained. The related PSCs have shown best devices with a power conversion efficiency of 18.22% and low hysteresis *J-V* curves (hysteresis index of 6.7%). Charge injection has been thoroughly studied by photoluminescence decay measurements. The decay curves followed a bi-exponential function. The injection of holes into the Spiro-OMeTAD layer was found very fast and is a no-limiting step. On the other side, the charge injection into the oxide ETLs depends on its structure and on the oxide. The time constants for the low-temperature SnO_2 layer are close to that of the mesoporous benchmark layers with a fast (surface) and slow (bulk) components at 11ns and 129 ns with relative contributions calculated at 13% and 87%, respectively. Phenomena occurring at longer time-scale have been investigated by impedance spectroscopy. The SnO_2 cell spectra showed no intermediate frequency inductive loop. The very low frequency part of the spectra was characterized by the beginning of an arc of circle at the origin of a very large resistance over a large applied potential range. This resistance, along with an intermediate frequency resistance, has been assigned to a recombination resistance and they explain the very large V_{oc} achievable with SnO_2 PSCs. The existence of a capacitance at intermediate frequency with a noticeable low value at about 0.2 $mF.cm^{-2}$ is linked with the low hysteresis of the devices.

Please cite this paper as : M. Ulfa, P. Wang, J. Zhang, J. Liu, W. Daney de Marcillac, L. Coolen, S. Peralta, T. Pauporté, Charge Injection and Electrical Response in Low Temperature SnO2-Based Efficient Perovskite Solar Cells. ACS Appl. Mater. Interfaces, 10 (2018) 35118–35128.
Keywords : Perovskite solar cells, SnO_2, TiO_2, Time resolved photoluminescence, Impedance spectroscopy, Electric model.

1. Introduction

Over the last few years, hybrid organo-lead perovskites (HPs) have emerged as one of the most promising family of materials for an application in highly performant opto-electronic devices.[1] These semiconductors have revolutionized the fields of light emitting diodes, lasers, photodetectors and photovoltaic solar cells.[1-18] The record efficiency for solar irradiation power conversion of the latter systems has raised rapidly to achieve a current certified world record of 22.7%.[19] In the most popular architecture delivering high efficiency and stable power output, a TiO_2 mesoporous structure, deposited on top of a TiO_2 hole blocking layer is employed.[20] The HP absorber layer is placed in-between this layer and a p-type one usually made of a molecular semiconductor. The oxide layer blocks the hole transfer and ensures the electron transport.[20] On the other side, the p-type contact layer blocks the electrons and ensures the transport of holes between the absorber and the back contact.[21,22] The drawback of TiO_2 is that it requires a high temperature sintering step (>450°C) which is incompatible with the fabrication at low cost and with flexible devices. On the other hand, there has been a lot of research effort to develop simplified devices without mesoporous layer with the planar n-i-p cell structures. The n-type oxide hole blocking layer is pivotal for planar PSC. Such kind of device employing TiO_2 electron transporting material (ETM) suffers from lower efficiency and large hysteresis of their *J-V* curves compared to the mesoscopic ones.

Recently, SnO_2 has emerged as the most promising n-type wide bandgap semiconductor to replace TiO_2 in planar PSCs.[23-33] The advantages of SnO_2 compared to TiO_2 are a deeper conduction band minimum, a wider bandgap (above 3.6 eV) and a high transparency over a large wavelength range as requested to maximize the solar light collected by the HP absorber. Moreover, SnO_2 has a high electron mobility (up to 240 $cm^2/(V.s)$ compared to $\approx 0.1-1$ $cm^2/(V.s)$ for TiO_2)[34-36] and it can be prepared at much lower temperature than TiO_2. In the literature, the main techniques employed for the preparation of SnO_2 layers are atomic layer deposition (ALD), spin-coating, chemical bath deposition (CBD) and electrodeposition.[23-33] In 2015, Baena et al.[24] fabricated planar PSCs based on SnO_2 layers formed by ALD at 120°C. They show that planar PSC using TiO_2 are inherently limited due to conduction band misalignment when SnO_2 achieves a barrier-free energetic configuration. These cells were almost hysteresis-free. Jiang et al.[25] developed the spin-coating of a colloidal solution of SnO_2 for the preparation of the SnO_2 layer. The layers were annealed at 150°C. A PCE close to 20% was achieved almost free of hysteresis. They suggested that the SnO_2 deep conduction band, the high electron mobility and then the reduction of the energy barrier at the perovskite/electron transporting layer (ETL) interface enhances the electron extraction and eliminates the *J-V* curve hysteresis. Mg –doping into high temperature proceeded SnO_2 yield better PCEs than the undoped ones.[26] The PSC *J-V* curve parameters

and PCE improvement was assigned to higher electron mobilities. Li-doping[27] and Al-doping[28] have also been reported to be beneficial for the PSC performances. Other works have focused on the SnO_2 surface engineering. Using a 3-aminopropyltriethoxysilane self-assembled monolayer (SAM) has demonstrated multifunction[29]: decrease of the work function of SnO_2 for an enlarged built-in potential; formation of high quality perovskite; passivation of trap states and hidering of electron back transfer and recombination reduction. On the other hand, surface fullerene layer has been described as promoting the electron transfer, passivating the SnO_2/perovskite interface and perovskite grain boundaries.[30] The use as the ETL of a SnO_2 layer two-step prepared (spin-coating and chemical bath deposition) and annealed at 180°C has resulted in PSCs with a V_{oc} as high as 1214 mV and a 20.7% PCE.[31] Electrodeposition has also been employed for SnO_2 ETL preparation. This solution-based (<100°C) processing method to synthesize crystalline SnO_2 has permitted to achieve a much lower PCE of 13.8%.[32] However, to our knowledge, in-depth investigations of the functioning and electrical response of efficient SnO_2-based PSCs are very scarce in the literature. A noticeable exception is the work by Guerrero et al..[37] These authors measured the impedance spectra of SnO_2 solar cells over a large applied potential range. The SnO_2 layer of the cell was prepared by ALD. However, they presented an inductive loop in the intermediate frequency range that we have reported as the signature of not optimized cells in our previous work.[20] This electrical feature could be due to aging since the cells were store several months before to be characterized.

In the present paper, we develop the preparation from a precursor aqueous solution of a low temperature (123°C) proceeded SnO_2 blocking layer which work efficiently, gives rise to a PCE as high as 18.2% and low hysteresis. Both $CH_3NH_3PbI_3$ and a methylammonium/formamidinium mixed cation hybrid perovskites (HPs) have been employed as solar light absorber materials.[14] We have investigated these structures to fully understand the remarkable effectiveness for charge carrier generation and collection. We have also investigated their electrical response to an ac signal by impedance spectroscopy in order to better understand the high efficiency and low hysteresis of the cells. A deep understanding has been achieved by comparing the SnO_2 planar solar cells with planar TiO_2 and mesoscopic TiO_2 solar cells. These comparisons have helped the interpretation of the results.

2. Experimental

The F-doped tin oxide coated glass (TEC7, Pilkington) was cut, and etched patterned using HCl 10% and Zn powder. It was then cleaned for 20 min in a concentrated 2.5 $mol.L^{-1}$ NaOH ethanolic solution, rinsed with water, cleaned with a detergent, rinsed with MilliQ water and dried with compressed air. The substrates were then annealed 30 min at 500°C on a hotplate.

The SnO_2 layer was prepared by spin-coating a precursor colloidal dispersion of tin (IV) oxide colloids (Alfa Aesar, 15% in H_2O) diluted to 2.35% with H_2O. This solution was stirred at least 30 min before use. 45 µL of this solution was spin-coated on the substrate at 3000 rpm for 30 s. and the layer was then annealed at 123°C for 1h30. This step was repeated then once. The TiO_2 blocking layer (noted *spr*-TiO_2) was prepared by an aerosol spray pyrolysis technique as described by some of us in Ref.16. A precursor solution was prepared by mixing 0.6 mL of titanium isopropoxide (TTIP), 0.4 mL of acetyl acetone in 7 mL of isopropanol. The substrate was placed on a hotplate at 455°C for 20 min prior to start spraying. The deposited layer was then annealed at 455°C for 40 min before to be let to cool down. The mesoporous TiO_2 layer was prepared on the *spr*-TiO_2 samples by diluting the NR30-D paste from Dyesol with ethanol (1:8 mass ratio). 40 µL of the solution was deposited on the blocking layer and spin-coated 20s at 5000 rpm. The layer was then dried on a hotplate at 100°C for 10 min and subsequently annealed at 500°C for 30 min under air flux. These samples and the related solar cells are noted *meso*-TiO_2.

The $FA_{0.83}MA_{0.17}Pb(I_{0.87}Br_{0.17})_3$ (FAMA) precursor solution contained 0.1719 g (1M) FAI, 0.0223 g (0.2M) MABr, 0.507 g (1.1M) PbI_2 and 0.0807 g (0.22 M) $PbBr_2$ dissolved in 0.8 mL a of N,N-dimethylformamide (DMF) (Sigma Aldrich) and 0.2 mL dimetyl sulfoxide (DMSO) (Alfa Aesar) solvent misture (4:1 volume ratio). 45µL of the perovskite precursor solutions was spin-coated on the oxide underlayers at 1000 rpm for 10 s (acceleration 200 rpm/s) and then at 6000 rpm for 35 s (acceleration 4000 rpm/s). During the second step, after 25s, 100 µL of chlorobenzene was dripped on the sample. The perovskite layer was finally annealed at 100 ºC for 1 h**.** The $CH_3NH_3PbI_3$ (MAPI) precursor solution was prepared by dissolving 461 mg of PbI_2 (TCI) and 159 mg of MAI (Dyesol) in 723 µL DMF and 81 µL DMSO. The molar ratio between PbI_2 and MAI was 1:1 and the concentration 1.24 M. 45 µL of this solution was spin-coated onto the SnO_2 layer by using a two-step program at 1000 rpm for 10 s and 4000 rpm for 20 s. During the second step, after 8s, 110 µL of chlorobenzene was slowly dripped onto the rotating substrate producing a surface aspect changed to turbid caused by the rapid vaporization of DMF. The perovskite film was finally heated at 105°C for 1h.[38,39]

The hole transporting material (HTM) solution was prepared by dissolving 72 mg of Spiro-OMeTAD (Borun New Material Technology) in 1 mL of chlorobenzene. Then, 17.5µL of bis(trifluoromethylsulfonyl)imide lithium salt solution (LiTFSI) (Sigma Aldrich) solution (520 mg in 1 mL ACN), 28 µL of TBP (tert-butylpyridine) (Sigma Aldrich) and 6 µL of tris(2-1H-pyrazol-1-yl)-4-tert-butylpyridine)-cobalt(III)-tris(bis(trifluoromethylsulfonyl)imide) (Dyesol, FK209) (300 mg in 1 mL acetonitrile) were added to this solution. 35 µL of the HTM solution was spin-coated at 4000 rpm for 20 s. Finally, the device was completed by thermally evaporating a 70-80 nm thick gold back contact on the Spiro-OMeTAD layer. The solar cell surface area delimited by the back contact was about 0.24 cm^2.

The *J-V* curves were recorded by a Keithley 2410 digital sourcemeter, using a 0.625 $V.s^{-1}$ voltage scan rate. The solar cells were illuminated with a solar simulator (Abet Technology Sun 2000) filtered to mimic AM 1.5G conditions.[40] The illuminated surface was delimited by a black mask with an aperture diameter of 3 mm. The power density was calibrated to 100 $mW.cm^{-2}$ by the use of a reference silicon solar cell.[41] The impedance spectra were measured at room temperature, between 600 kHz and 20 mHz, using a PGSTAT 20 apparatus from Autolab. All the measured cells had the same contact geometries. The AC signal was 20 mV. All the impedance spectra were measured at room temperature, over a large applied voltage range under a ~1 sun light power provided by a halogen Schott lamp.[42] These spectra were analyzed using the Z-view software from National Instrument.

The scanning electron microscopy (SEM) experiments were performed on a GeminiSEM 300 from ZEISS. The images were acquired at 5kV with the In-lens SE detector. Samples did not undergo any treatment. The atomic force microscopy (AFM) experiments were performed in the Peak Force QNM mode with a Dimension ICON microscope from Bruker. Measurements were carried out in air at room temperature with a tip model ScanAsyst (k = 0.4 N/m, Bruker). The structure of the organolead perovskite film was characterized by a PANanalytical X-Pert high-resolution X-ray diffractometer (XRD) operated at 40 kV and 45 mA and using the CuK_α radiation with λ = 1.5406 Å. The film specular absorbance was measured by a Cary 5000 UV-Vis-NIR spectrophotometer. The photoluminescence (PL) measurements were performed under microscope observation (numerical aperture 0.7). The PL spectra and decay curves of the perovskites were studied on layers spin-coated on glass substrate, on layers deposited on the oxide ETLs and on layers deposited on glass and covered by the Spiro-OMeTAD layer. The HPs were excited by a 470 nm diode laser (Picoquant) either directly or through the Spiro-OMeTAD covering the FAMA layer on glass. The emission was filtered by a 488-nm longpass filter and analyzed either (i) for photoluminescence spectra, by a Horiba Triax 190 monochromator and a QImaging Retiga EXi CCD camera, used with 0.24 µW continuous excitation power or (ii) for photoluminescence decay, by a PerkinElmer SPCM avalanche photodiode combined with a Picoharp acquisition card (500 ps characteristic time of the total system response function) used with the laser in a pulsed mode at a 0.14 µW excitation power (pulse duration 70 ps).

3. Results and discussion

The developed SnO_2 layer was prepared by spin-coating and we focused our study on an optimized layer for which the annealing temperature was as low as 123°C. Figure 1a and 1b show SEM views of the bare SnO_2 substrate and of the substrate after the deposition of the SnO_2 layer, respectively. The FTO layer was made of large grains with an average size of 200-250 nm. After the SnO_2 coating and annealing, the aspect of the surface changed significantly and the FTO underlayer was covered by a

featureless layer of SnO_2. The layer was crack-free. Further morphological characterizations were carried out by the AFM technique. Pictures in Figure 1(c,d) show that the SnO_2 layer deposition occurred preferentially at the troughs of the FTO grains and a consequence was the obliteration of the FTO underlayer. This effect has been quantified by measuring the change in surface roughness defined as the ratio between the scanned surface over the projected geometrical areas. This parameter was reduced from 1.215 to 1.12 after SnO_2 deposition and at the same time, the root-mean-squared roughness of the layer decreased from 38.9 nm to 23.6 nm. It is interesting to compare these layers to the optimized TiO_2 layer developed for the application by some of us and prepared by spray pyrolysis. Its optimization has been reported in the previous work of some of us.[20] Figure 1e is a SEM top view of the *spr*-TiO_2 blocking layer which perfectly conformaly covers the FTO substrate. More characterizations are available in Ref.[20].

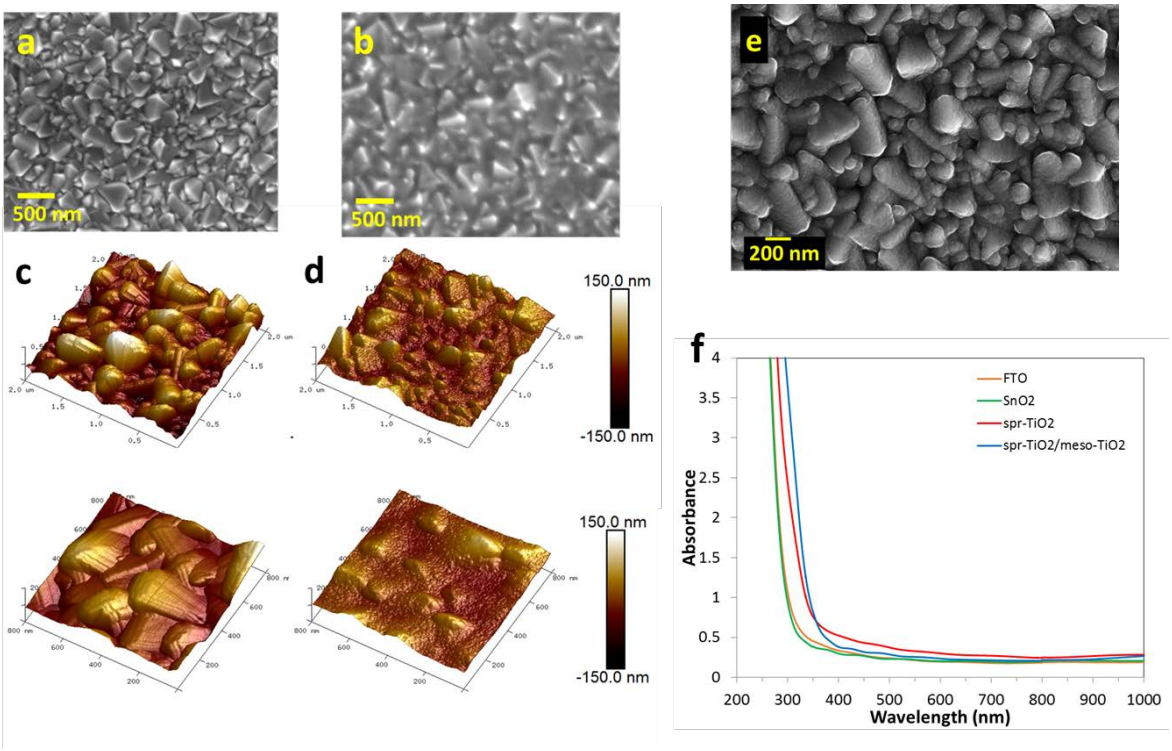

Figure 1. SEM top views of the (a) bare FTO substrate and (b) after the SnO_2 layer deposition. AFM images of (c) the bare FTO substrate and (d) after the SnO_2 layer deposition: (top) : 2µm x 2µm image; (bottom): 800 nm x 800 nm image (the vertical scale was 300nm for all images). (e) SEM top view of the sprayed TiO_2 layer (*spr*-TiO_2). (f) Absorbance spectra of the bare FTO substrate and SnO_2, *spr*-TiO_2 and *meso*-TiO_2 layers on FTO.

The optical properties of the oxide layers were characterized by measuring their absorbance curves. Figure 1f compares the SnO_2 layer with the *spr*-TiO_2 layer and *spr*-TiO_2/*meso*-TiO_2 bilayer. The specular absorbance of the SnO_2 layer is close to the substrate FTO/glass sample and its absorption edge

lies below 350 nm. They are highly transparent over the visible/near infra-red wavelength spectral range. On the other hand, the sprayed TiO_2 has an absorption edge red-shifted compared to the *spr*-SnO_2 layer due to the lower bandgap of TiO_2. The absorbance edge analysis resulted in an indirect bandgap of *spr*-TiO_2 measured at 3.45 eV (Figure S1, Supporting Information). In Figure 1f, the *spr*-TiO_2/meso-TiO_2 bilayer absorbance spectrum presents lower absorbance in the visible region compared to the other samples due to less diffuse light and more specular transmission. The absorption edge is slightly shifted and the Tauc analysis in Figure S1 (Supporting Information) gives an optical bandgap at 3.15 eV.

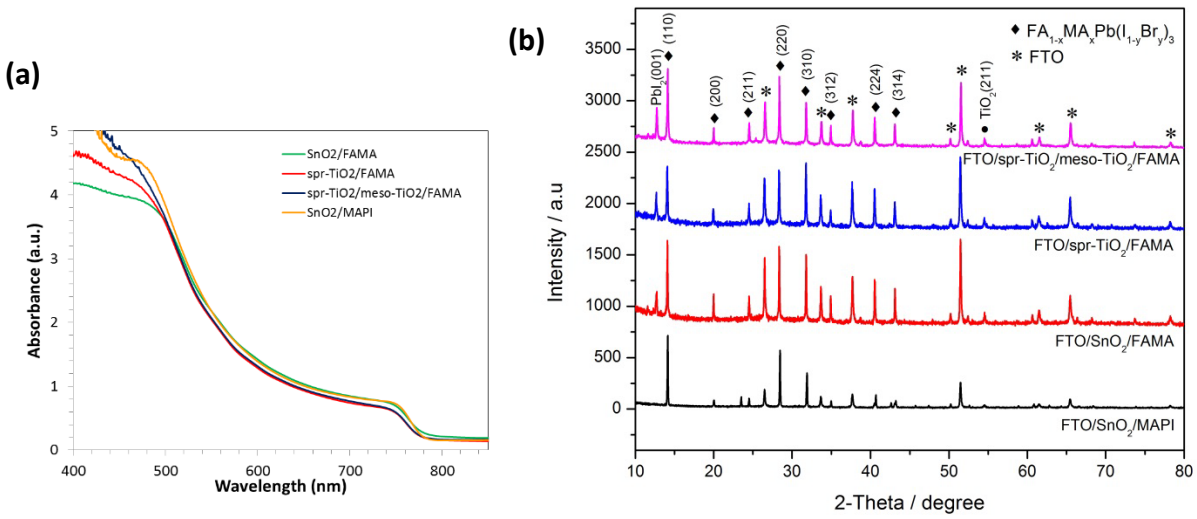

Figure 2. (a) Absorbance spectra and (b) XRD patterns of FAMA and MAPI layers prepared on various oxide ETLs.

The absorbance spectra of FAMA and MAPI deposited on various oxide substrates are shown in Figure 2a. The organo-lead halide compounds absorb across the whole visible region with an edge at 780 nm. Figure 2a shows that FAMA is slightly more absorbing when prepared on the SnO_2 underlayer compared to the TiO_2 ones. The main difference between the spectra occurs below 500 nm. We also observe that the MAPI absorbance curve is close to that of the FAMA curves. A zoom view of the absorption edge shows a slightly steeper edge in the case of MAPI compared to FAMA (Figure S2a, Supporting Information). The Tauc plot gives a direct optical bandgap (E_g) at 1.59 eV-1.60 eV for both FAMA and MAPI (Figure S2b, Supporting Information). The structural characteristics of the HP samples are shown in Figure 2b. XRD patterns are indexed with the tetragonal HP structure peaks and those of the FTO substrate. The perovskite is well-crystallized. For FAMA, we note the presence of the (001) PbI_2 diffraction peak at 12.7° in all cases. The intensity of this peak and the crystallinity of the HP are similar for the *spr*-TiO_2/FAMA and *spr*-TiO_2/*meso*-TiO_2/FAMA samples showing that the meso-TiO_2 layer has no influence on the FAMA compound. On the other hand, the PbI_2 peak is less intense on SnO_2 compared to TiO_2 and then less PbI_2 impurity is formed on this substrate. The first stages of

the perovskite formation, that are its nucleation and initial growth, are influenced by the interaction of the precursors with the oxide substrate and then is influenced by its chemical nature. It is noteworthy that MAPI on SnO_2 is pure phase with no PbI_2 impurity (Figure 2b). The perovskite surface morphology has been probed by AFM (Figure S3a, Supporting Information). Larges grains are observed for MAPI. FAMA on SnO_2 and meso-TiO_2 have a similar aspect. The roughness quantification yields similar values for the various FAMA samples (Figure S3b, Supporting Information). The MAPI layer on SnO_2 is smoother and the layer is made of large grains with a 210 nm mean size. The FAMA grains have similar size, ranging between 126-155 nm, for the various oxide underlayers.

Cells have been prepared by completing these structures by a doped Spiro-OMeTAD layer and by a gold back contact. The planar architecture (Figure 3a) has been used for SnO_2 and *spr*-TiO_2, whereas, for the sake of comparison, we have also studied in parallel the mesoscopic TiO_2 cells (*meso*-TiO_2) which structure is presented in Figure 3b. Figure 3c is a cross-sectional view of the planar SnO_2/FAMA cell. It shows the large grains of FAMA and the absorber layer thickness is estimated at 380 nm. The cells have been electrically characterized under one sun illumination by measuring their *J-V* curves under reverse and forward voltage scan directions. The results are gathered in Table 1 and Figure 3d shows the *J-V* curves for the best cells.

Table 1. Photovoltaic parameters of SnO_2-based, TiO_2-based planar solar cells and of meso-TiO_2 based solar cells under 100 mW.cm^{-2} AM 1.5G illumination. The numbers in brackets are the standard deviations.

		V_{oc} (V)	J_{sc} (mA.cm^{-2})	FF (%)	PCE (%)	HI (%)[a]
SnO_2 planar (FAMA)	**Max (Rev)**	**1.05**	**23.03**	**75.44**	**18.22**	**6.7**
	Max (For)	**1.04**	**23.02**	**71.21**	**17.03**	
	Avg (Rev)	1.04 (0.01)	22.79 (0.44)	72.61 (4.36)	17.18 (1.44)	6.7
	Avg (For)	1.03 (0.01)	22.76 (0.48)	68.19 (3.75)	16.06 (1.22)	
SnO_2 planar (MAPI)	**Max (Rev)**	**1.01**	**21.92**	**68.84**	**15.28**	**23.4**
	Max (For)	**0.97**	**21.98**	**56.40**	**12.08**	
	Avg (Rev)	1.01 (0.03)	20.25 (1.72)	62.22 (4.76)	12.71 (1.83)	18.6
	Avg (For)	0.97 (0.02)	20.91 (0.89)	52.02 (3.10)	10.55 (1.08)	
TiO_2 planar (FAMA)	**Max (Rev)**	**1.01**	**22.49**	**77.50**	**17.65**	**52.8**
	Max (For)	**0.90**	**22.43**	**50.86**	**10.28**	
	Avg (Rev)	1.01 (0.02)	20.71 (1.12)	66.91 (8.60)	14.08 (2.14)	61.2
	Avg (For)	0.94 (0.03)	20.59 (1.19)	38.64 (10.44)	7.48 (1.89)	
TiO_2 meso (FAMA)	**Max (Rev)**	**1.02**	**24.05**	**76.1**	**18.67**	**36.4**
	Max (For)	**1.01**	**23.24**	**55.02**	**12.92**	
	Avg (Rev)	1.01 (0.008)	23.34(0.665)	75.93(1.33)	17.93(0.49)	43.2
	Avg (For)	0.989(0.0136)	23.27(2.60)	50.72(2.60)	11.55(0.823)	

a) $\mathrm{HI}(\%) = \dfrac{(\mathrm{PCE})_{\mathrm{REV}} - (\mathrm{PCE})_{\mathrm{FOR}}}{(\mathrm{PCE})_{\mathrm{AVG}}}$ with $(PCE)_{REV}$, $(PCE)_{FOR}$ and $(PCE)_{AVG}$ the power conversion efficiencies determined on the reverse scan, forward scan and by averaging both, respectively.

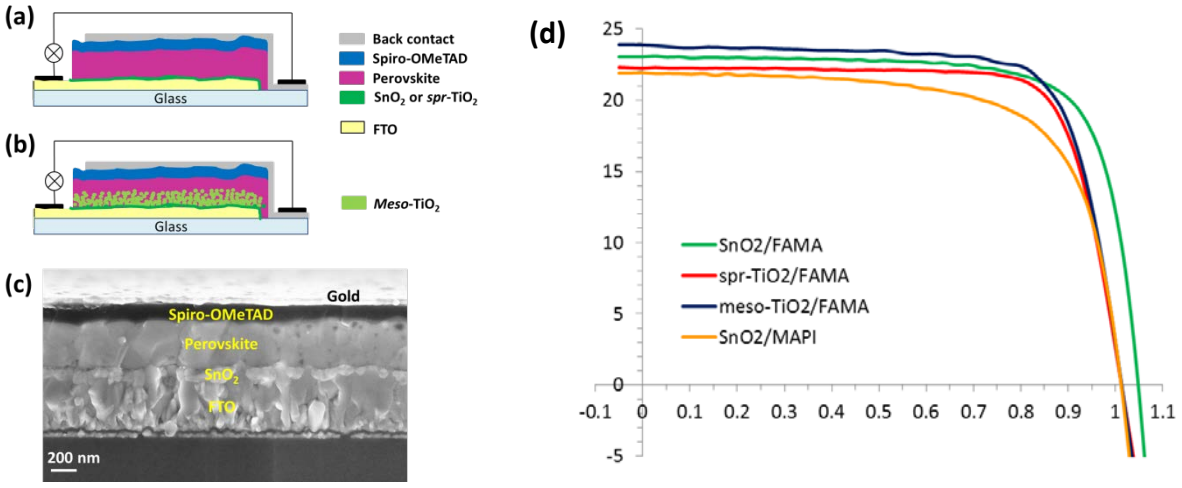

Figure 3. (a) Planar and (b) mesoscopic PSC architectures. (c) Cross-sectional SEM view of a planar SnO_2/FAMA solar cell. (d) *J-V* curve under simulated AM 1.5 G illumination of the best cells with various assemblies.

In Table 1, the *J-V* curve parameters and the PCE of cells prepared using the SnO_2 ETL combined with either FAMA or MAPI are reported. Actually, SnO_2/FAMA cells presented high performances, with a PCE reaching more than 18.2 %. Interestingly, these cells were almost hysteresis-free (hysteresis index, HI, at 6.7%) (Table 2 and Figure S4, Supporting Information).[22] These cells were also characterized by a high V_{oc}. It has been pointed out by some authors that the bottom of the conduction band of the HP must be closely aligned to the CB of SnO_2 to reach such high V_{oc}.[24]

With MAPI, the efficiency was lower at 15.28 % and the hysteresis was rather high (HI at 23% for the best cell). Compared to the SnO_2/FAMA cells, the three *J-V* curve parameters were degraded and it suggests a worse energy matching and more recombination in this case.

SnO_2 cells have been compared to TiO_2 cells. We have found that the maximum PCE of the meso-TiO_2 cells (18.67 %) was higher than with SnO_2 but the hysteresis was much larger (HI equal to 36 %). Moreover, the key advantages of the planar SnO_2 cells are a simplified structure and a low temperature processing. Actually, the SnO_2 layer was annealed at a temperature as low as 123°C which is compatible with substrates that do not stand high temperature such as the plastic ones. In Table 1, we also report the performances of planar TiO_2 cells. If the performances were high (maximum at 17.65 %), these cells suffered from a very large hysteresis. This behavior is completely different to the one of the planar SnO_2 devices which showed a low HI.

Photoluminescence measurements can substantially improve our understanding of the complex nature of charge-carrier processes in metal-halide perovskites. These technologies have been implemented to study the charge injection at the selective contacts and to understand the effect of the oxide ETM and layer assemblies on the cell performances. Time integrated PL spectra of FAMA supported on various substrates are reported in Figure 4a. They are characterized by an emission centered at 774 nm. The maximum emission is measured for the FAMA layer deposited on blocking glass substrate. The PL intensity is lowered in the presence of an ETL due to charge transfer. Higher transfer is found for a contact made of planar SnO_2 compared to the planar *spr*-TiO_2 layer. This indicates a much efficient charge separation in the case of the SnO_2 contact. Figure 4a also shows that adding the mesoporous layer improves dramatically the quenching of the FAMA photoluminescence. Indeed, the mesoporous layer increases dramatically the contact area with FAMA. Also, this layer likely has a beneficial effect to optimize the energy barrier and contact between the two layers. The effect of the various selective contacts has also been investigated by time-correlated single-photon counting (TCSPC) measurements. The curves are displayed in Figure 4b and in Figure S5 (Supporting Information). They have been fitted with a bi-exponential decay function as described in the Section-A of the Supporting Information. The luminescence decay dynamics reflected by the fast-decay component, τ_{fast}, was assigned to free-carrier recombination at the surface and the slow-decay component τ_{slow} was assigned to the free-carrier recombination in the bulk for carriers propagating deeper in the material.[43,44] The measured values for the various systems are gathered in Table 2. For pristine FAMA on glass, a fast lifetime constant was found at 82 ns and a slow one at 620 ns with a very high relative contribution (RC) of the latter (90.4%). The large values obtained show the good quality of the prepared perovskite material. For pristine MAPI we found τ_{fast}=29 ns and τ_{slow}=301 ns (Table 2). The fast component was close to the bulk single crystal one measured at 22 ns in Ref.[43] while the slow lifetime was much shorter at 301 ns (while 1032 ns was reported for MAPI single crystal[43]). Higher carrier lifetime for FAMA confirms that this material is better suited for high efficiency due to less defects. Contacting FAMA to Spiro-OMeTAD had a dramatic effect on the decay curve (Figure S5, Supporting Information). The carrier lifetimes were then measured at 2 ns (46% RC) and 88 ns (54% RC) (Table 2). It shows a highly efficient charge injection into the HTM. For the ETM contact, the SnO_2 planar layer was found to act efficiently since the time constants of FAMA decreased markedly when it was stacked with this material (11 ns and 129 ns) (Table 2). Planar SnO_2 is shown much more efficient than the planar *spr*-TiO_2 contact for which time constants were higher. Interestingly, our experiments show that a mesoporous TiO_2 layer is required to get highly efficient electron injection into TiO_2. Then, a slightly better charge injection than for SnO_2 was attained. It can explain the higher photocurrent achieved for the former cells (Figure 3d and Table 1). The highly efficient electron transfer from FAMA toward the SnO_2 layer developed here is remarkable since this oxide layer was prepared from a precursor solution at low temperature (123°C), whereas the *meso*-TiO_2 bilayer required high temperature

annealing up to 455°C to operate more efficiently. Therefore, SnO_2 appears as the most interesting oxide ETM for the fabrication of efficient planar and flexible cells.

We have also employed the PL techniques to investigate the electron injection from MAPI to SnO_2. The spectra and decay curves are presented in Figure S6a and S6b (Supporting Information), respectively. The PL spectra are centered at about 770 nm and their intensity is reduced by the presence of the SnO_2 layer due to the ability of the SnO_2 to collect electronic charges. The MAPI TCSPC curves have been fitted by a biexponetial decay function which parameters are gathered in Table 2. The two time constants are markedly shortened when MAPI is contacted by the SnO_2 layer and therefore SnO_2 allows the charge separation for the electrons photogenerated in MAPI.

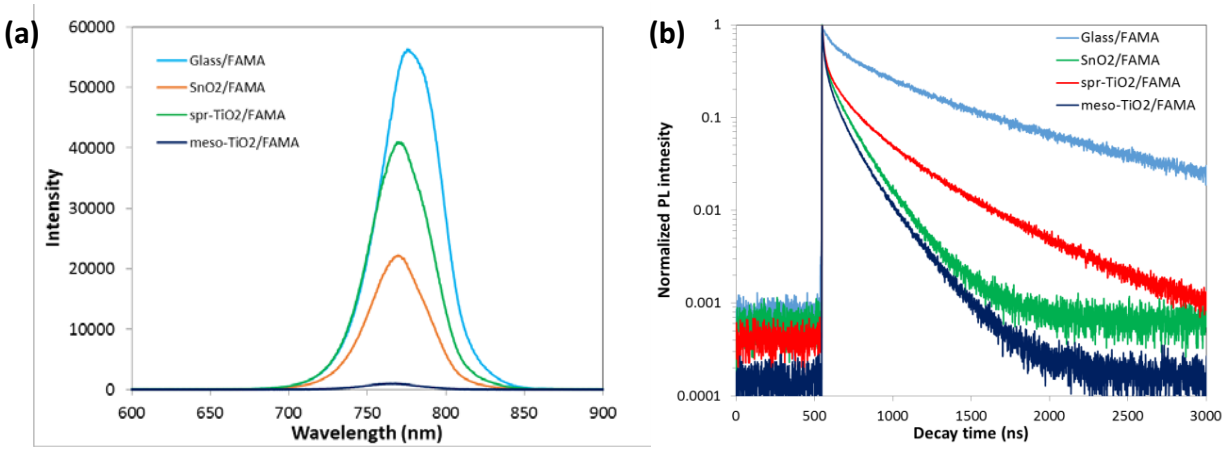

Figure 4. (a) Emission spectra of the FAMA layer on glass and supported on various oxide substrates. (b) Time-correlated single-photon counting curves of the photoluminescence. Same samples as (a).

Table 2. Parameters of PL decays determined from the bi-exponential TCSPC curve fitting. Fast and slow lifetimes and relative contributions of the fast and slow components.

Perovskite	**Sample**	**τ_{fast} (ns)**	**RC_{fast}(%)[a]**	**τ_{slow} (ns)**	**RC_{slow}(%)[a]**
FAMA	Glass/FAMA	82.0	9.6	619.8	90.4
	SnO_2/FAMA	11.1	12.6	128.7	87.4
	spr-TiO_2/FAMA	15.9	12.6	233.8	87.4
	Meso-TiO_2/FAMA	11.8	16.9	113.7	83.1
	Spiro/FAMA	1.98	45.8	17.7	54.2
MAPI	Glass/MAPI	28.7	17.2	300.9	82.8
	SnO_2/MAPI	4.8	0.9	110.1	99.1

[a] Relative contribution (see section A-Supporting Information for its definition and calculation).

To gain deeper insights into the effects of the ETL oxide material and architecture on the cell functioning and electrical response, the various devices were thoroughly investigated by impedance spectroscopy (IS). In the recent years, various works have shown that IS is a powerful technique for the investigation of PSCs.[14,20,42,45-57] For instance, we have employed this non-destructive technique to investigate various TiO_2 blocking layers,[20] the use of various monovalent cations in the organo-lead perovskite,[14] the effect of doping of the HTM on the PSC functioning[21,22] and so on. The phenomena of charges (ions, electrons/holes) transfer and accumulation can be thoroughly investigated and followed by IS. The cells were analyzed under light illumination, over large applied voltage and frequency ranges. Figure 5a-d show Nyquist plots of spectra recorded in the 600 kHz-20 mHz range at 0.0V and 0.6V applied voltages. The spectra of the whole cells were characterized by two main loops. One can point out that our SnO_2 cells did not show an inductive loop at the intermediate frequency. It confirms that large intermediate frequency inductive loop is a signature of poorly working cells. On the Nyquist plots, we can note that the low frequency loop had a different shape in the case of the SnO_2/FAMA cells with a rise below 1Hz which draw the beginning of a new loop. To better distinguish the various resistance and capacitance features in the spectra, other spectral representations have been employed. Figure 5e and 5f are the real part of the complex impedance as a function of the frequency for an applied potential of 0.0V and 0.6V, respectively. Three main resistive features are observed. At very high frequency, R_s is the series resistance due to wires and the resistances of the contacts. We also note the presence of a plateau at 100Hz-2kHz which corresponds to the high frequency resistance R_2, defined by the first arc of circle. A low frequency resistance is defined by extrapolating the spectra at very low frequency. The very low frequency behavior of SnO_2/FAMA results in a large resistance at the steady state and then a high FF.

We have also calculated the complex capacitance of the spectra defined as:

$$C^*=C'+iC''=\frac{1}{Zi\omega} \qquad (1)$$

with *i* the square root of -1 and ω the angular frequency related to the ordinary frequency as $f=\omega/2\pi$. Figure 5g and 5h figure out the real part of the complex capacitance (C') for the various cells at 0.0V and 0.6V applied voltages. A first capacitive process is found at high frequency. It defines the capacitance C_2. This parameter does not change significantly for the various cells and it is now well-assigned to the bulk capacitance of the perovskite.[14,20-22,37] Interestingly, we note on these figures a different shape for both FAMA/SnO_2 and MAPI/SnO_2 cells, with a capacitive feature in the 0.5Hz-10Hz region which is noted C_3. At very low frequency, C_4 is defined for all the cells.

Please cite this paper as : M. Ulfa, P. Wang, J. Zhang, J. Liu, W. Daney de Marcillac, L. Coolen, S. Peralta, T. Pauporté, Charge Injection and Electrical Response in Low Temperature SnO2-Based Efficient Perovskite Solar Cells. ACS Appl. Mater. Interfaces, 10 (2018) 35118–35128.

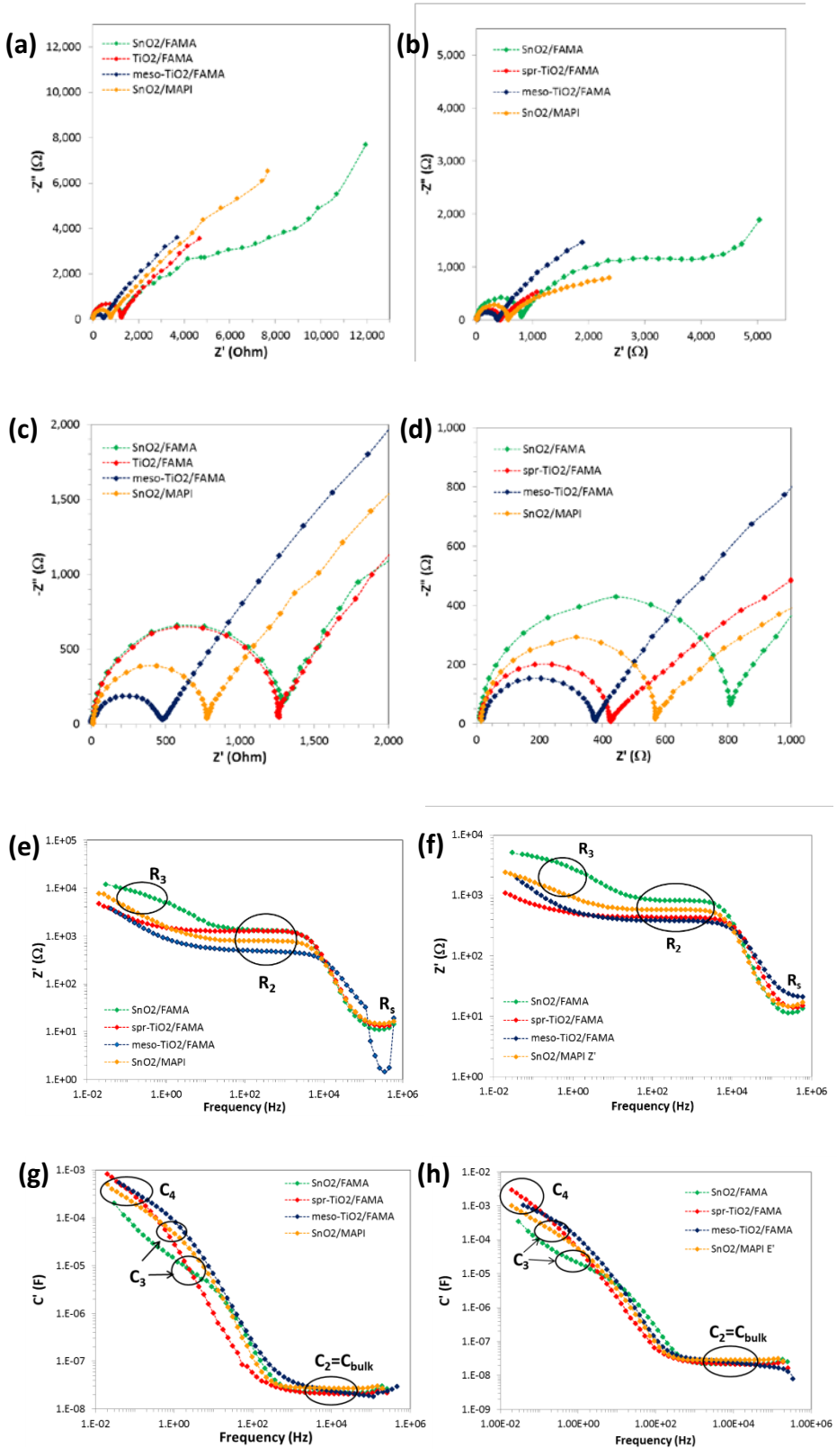

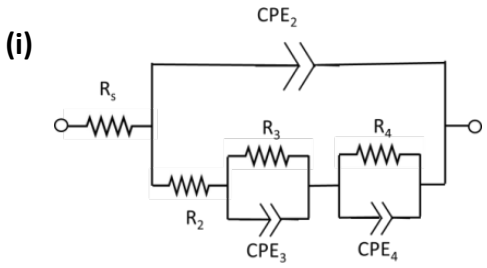

Figure 5. (a,b) Nyquist plots of the impedance spectra of cells with various ETL and HP assemblies. (c,d) High frequency zoom views of the spectra. (e,f) Real part of the complex impedance plotted versus the frequency. (g,h) Real part of the complex capacitance plotted versus the frequency. (a,c,e,g) Applied potential: 0.0V; (b,d,f,h) Applied potential: 0.6V. (i) Full equivalent electrical circuit used to fit the impedance spectra.

Based on these observations, the full electrical equivalent circuit (ECC) used to fit the spectra is presented in Figure 5i. Because the arcs of circle are not semicircles, they have been fitted using R//CPE circuits with CPE being a constant phase element. The actual capacitances were extracted from the CPE parameters as described in our previous works.[14,20-22] The various resistances and capacitances have been determined from the spectrum fits and plotted as a function of the applied voltages. R_2 is the high frequency resistance, plotted in Figure 6a. This parameter can vary in a large extent for cells with the same absorber (FAMA). It also varies in a large extent for cells with the same ETM layer and different HP. For instance SnO_2/FAMA and SnO_2/MAPI curves have the same shape but R_2 is lower for MAPI compared to FAMA while they involve the same ETL. Therefore this resistance is complex and gathers several contributions. From our results it is clear that the main one is related to the interface between the oxide and the perovskite. Some authors have suggested that this resistance is a recombination resistance. In the present case, the curves for the SnO_2 cells, with higher resistances for the SnO_2/FAMA cells which deliver a higher J_{sc} and FF, could be consistent with that interpretation. On the other hand, R_2 of the TiO_2 cells would be more complex.

R_3 and R_4 could be determined accurately in the case of the TiO_2 cells and of the SnO_2/MAPI cell. For the SnO_2/FAMA cell the upward bending of the spectra observed at very low frequency rendered the determination of R_4 difficult and this parameter was underestimated in this case. The variation of R_3 with the applied potential is shown in Figure S7 (Supporting Information). We suggest that R_3 and R_4 are recombination resistances. Their sum, plotted in Figure 6b, provides a good estimation of the recombination phenomena in the cells: the higher this parameter, the lower the recombinations. The curve of the SnO_2/MAPI cell decreases more rapidly than those of the other cells and is in good agreement with the lower FF in this case. Adding the mesoporous layer to the *spr*-TiO_2 one has a beneficial effect since it gives rise to higher resistances in good agreement with the higher performances

of these cells. We can suppose that the presence of the mesoporous layer improves the HP crystal formation and that the quality of the interface with TiO_2 is better due to less surface states.

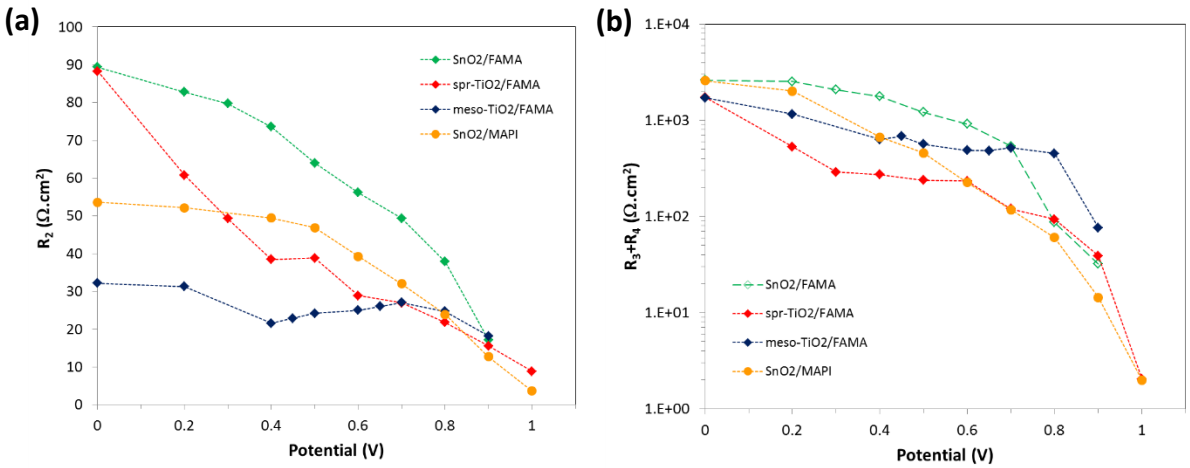

Figure 6. Variation of the solar cell resistance measured under light at various applied potentials. (a) R_2; (b) R_3+R_4.

Based on our previous IS studies of perovskite solar cells, C_2 is assigned to the dielectric capacitance of the perovskite.[14,20-22,37] The HP absorbance curves (Figure 3a) were about the same for the various cells and then the equivalent HP thickness was close for the various systems. The higher C_2 of SnO_2/MAPI cell compared to SnO_2/FAMA is in good agreement with our previous results and shows a higher ε_r (relative permittivity) for MAPI compared to FAMA. Lower C_2 in the presence of meso-TiO_2 can be related to the presence of the porosity. The C_3 capacitance is clearly observed on the C'=f(Hz) curve (Figure 5g,h) for the planar SnO_2 cells. This parameter has been determined for these cells and is plotted as the function of the applied voltage in Figure 7b. The main feature is the low value of this capacitance in the case of SnO_2/FAMA. This observation can be correlated with the cell hysteresis results. Actually, the scan rate for the $J-V$ curve measurement corresponds to an impedance frequency in the hertz range and at these frequencies the SnO_2/FAMA cell has a capacitive behavior with a low capacitance value, in agreement with a small hysteresis. C_4 is the very low frequency capacitance and has large values in every cases. It is plotted in Figure 7c and heavily varies with the applied potential. C_3 and C_4 could be accumulation capacitances. They are controlled by ionic defects and proportional to the amount of charge, but charge accumulation must be compensated for by moving ions, which is actually the reason why its effect is detected at lower frequencies instead of a higher one, as should be expected for electronic phenomena.[57]

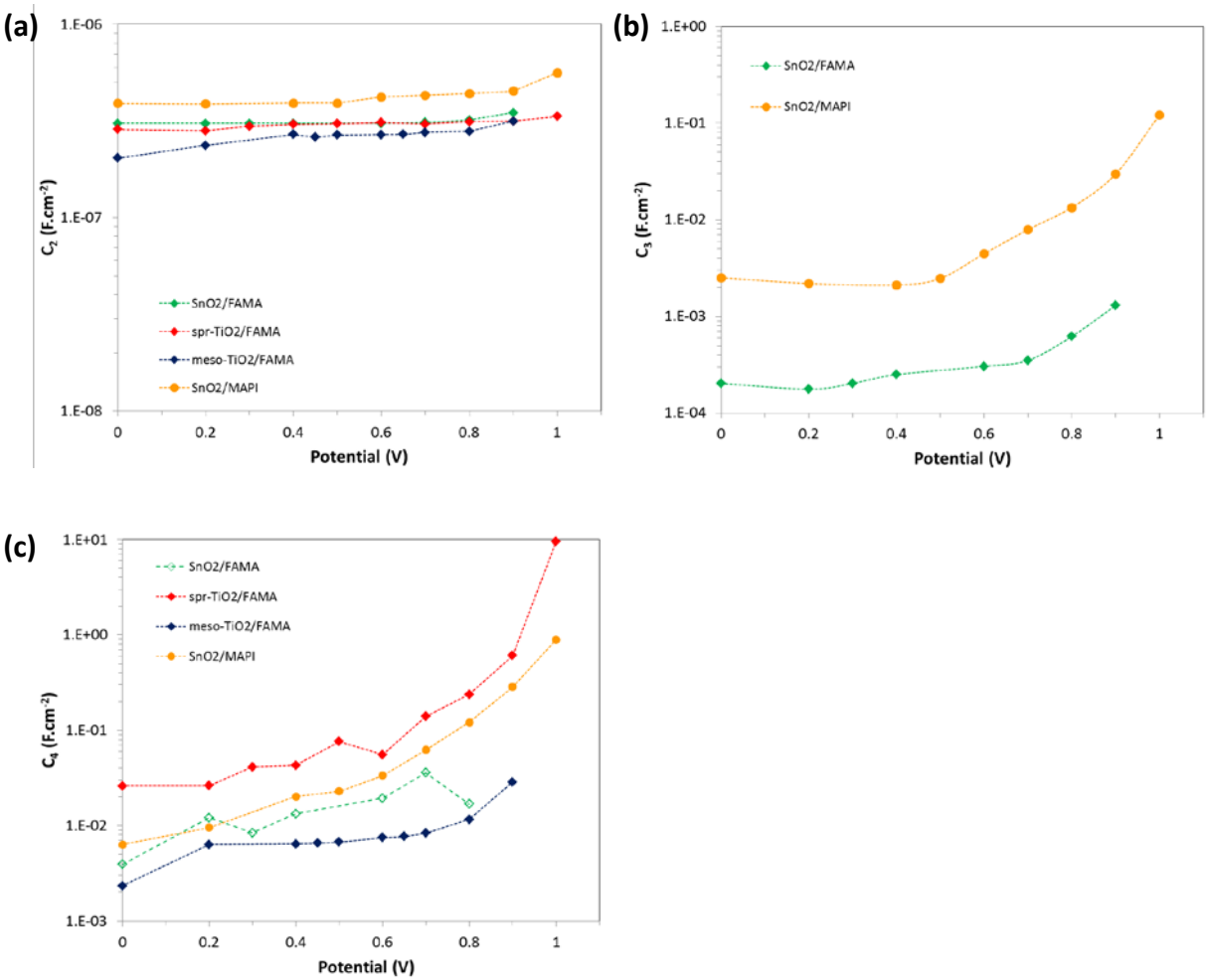

Figure 7. Variation of the solar cell capacitances measured under light at various applied potentials. (a) C_2; (b) C_3; (c) C_4. Note that C_4 (green open symbol) for SnO_2/FAMA is poorly-estimated due to a very low relaxation frequency IS feature.

Conclusions

In conclusion, we have defined a low-temperature (123°C) protocol using a colloidal solution of SnO_2 for the preparation by twofold spin-coating of an efficient ETM layer for perovskite solar cells. The layer was crack-free and correctly covered the FTO substrate. The deposition occurred preferentially at the troughs of the FTO grains and the layer was highly transparent throughout the near-UV and visible range. Planar cells have been prepared based on this layer and MAPI and FAMA perovskites. With FAMA absorber, the devices were highly efficient with a maximum PCE of 18.2% and an almost hysteresis-free behavior (6.7% HI). PL spectra measurements and TCSPC experiments have shown the very fast hole transfer from the perovskite layer into the Spiro-OMeTAD layer. The charge carrier injection was slower on the ETM side. Actually, TCSPC has shown that the electron transfer is highly dependent on the oxide used and its morphology. The planar SnO_2 layer permitted a

fast and efficient electron transfer, much faster than the planar TiO_2. Moreover, the TCSPC technique also showed the less defective nature of the FAMA perovskite compared to the MAPI one. Phenomena occurring at longer time scales have been investigated by the impedance spectroscopy technique. The spectra were free of inductive loop. They have been fitted with an *ad-hoc* equivalent electrical circuit. Our results confirm that the well-working perovskite solar cells are free of significant intermediate frequency inductive loop. The R_2 resistance has been shown to be complex and to combine several phenomena. The low frequency resistances R_3 and R_4 have been assigned to the recombination phenomena occurring at the contacts with the perovskite layer. For the SnO_2/FAMA cells, the very low frequency part of the spectra was characterized by the beginning of an arc of circle at the origin of a very large R_4 over a large applied potential range which explains the very large V_{oc} achievable with SnO_2 PSCs.[31] The complex capacitance spectra of the SnO_2-based solar cell showed the presence of intermediate C_3 and low frequency C_4 capacitances. The low-hysteresis in the *J-V* curves of the SnO_2/FAMA cells has been linked with the capacitive behavior of the device in the 0.5-10 Hz range (C_3 capacitance) which values were noticeably low.

Supporting Information

The Supporting Information is available free of charge on the ACS Publications website at DOI: 10.1021/acsami

Tauc plots of oxide layers; Absorbance curves and Tauc plots of the perovskite layers; Forward and reverse scan *J-V* curves of the SnO_2/FAMA cell; TCSPC of FAMA/Spiro-OMeTAD; PL and TCSPC of MAPI layers; Fitting of the time resolved photoluminescence curves; Variation of the R_3 parameter with the applied voltage.

Acknowledgements

M.U. acknowledges the Indonesia Endowment Fund for Education (LPDP) scholarship for funding (grant PRJ-2060/LPDP/2015). T.P. and J. Z. Acknowledge the National Natural Science Foundation of China (Project number: NSFC 21703070) for financial support.

References

(1) Veldhuis, S.A.; Boix, P.P.; Yantara, N.; Li, M.J.; Sum, T.C.; Mathews, N.; Mhaisalkar, S.G. Perovskite Materials for Light-Emitting Diodes and Lasers. *Adv. Mater.* **2016**, *28*, 6804-6834.

(2) Kim, H.S.; Lee, C.R.; Im J.H.; Lee, K.H.; Moehl, T.; Marchioro, A.; Moon, S.J.; Humphry-Baker, R.; Yum, J.H.; Moser, J.E.; Gratzel, M.; Park, N.G.. Lead Iodide Perovskite Sensitized All-Solid-State Submicron Thin Film Mesoscopic Solar Cell with Efficiency Exceeding 9%. *Sci. Rep.* **2012**, *2*, 591.

(3) Lee, M.M.; Teuscher, J.; Miyasaka, T.; Murakami, T.N.; Snaith, H.J. Efficient Hybrid Solar Cells Based on Meso-Superstructured Organo-Metal Halide Perovskite. *Science* **2012**, *338*, 643-647.

(4) Liu, M.; Johnston, M.B.; Snaith, H.J. Efficient Planar Heterojunction Perovskite Solar Cells By Vapour Deposition. *Nature* **2013**, *501*, 395-398.

(5) Burschka, J.; Pellet, N.; Moon, S.J.; Humphy-Baker, R.; Gao, P., Nazeeruddin, M.K.; Grätzel, M. Sequential Deposition as a Route to High-Performance Perovskite-Sensitized Solar Cells. *Nature* **2013**, *499*, 316-319.

(6) Zhang, J.; P. Barboux, P.; T. Pauporté, T. Electrochemical Design of Nanostructured ZnO Charge Carrier Layers for Efficient Solid-State Perovskite-Sensitized Solar Cells. *Adv. Energy Mater*. **2014**, *4*, 1400932.

(7) Nie, W.Y.; Tsai, H.H.; Asadpour, R.; Blancon, J.C.; Neukirch, A.J.; Gupta, G.; Crochet, J.J.; Chhowalla, M.; Tretiak, S.; Alam, M.A. High-Efficiency Solution-Processed Perovskite Solar Cells with Millimeter-Scale Grains. *Science* **2015**, *347*, 522-525.

(8) Zhang, J.; Juárez-Pérez, E. J.; Mora-Seró, I.; Viana, B.; Pauporté, T. Fast and Low Temperature Growth of Electron Transport Layers for Efficient Perovskite Solar Cells. *J. Mater. Chem. A.* **2015**, *3* 4909–4915.

(9) Zhang, J.; Pauporté, T. Effect of Oxide Contact Layer on the Preparation and Properties of $CH_3NH_3PbI_3$ for Perovskite Solar Cell Application. *J. Phys. Chem. C* **2015**, *119*, 14919−14928.

(10) Zhang J.; Pauporté, T. One-Dimensional Free-Standing TiO_2 Nanotube Arrays Designed for Perovskite Solar Cells Application. *ChemPhysChem*, **2015**, *16*, 2836–2841.

(11) You, J.B.; Meng, L.; Song, T.B.; Guo, T.F.; Yang, Y.; Chang, W.H.; Hong, Z.R.; Chen, H.J.; Zhou, H.P.; Chen, Q. Improved Air Stability of Perovskite Solar Cells via Solution-Processed Metal Oxide Transport Layers. *Nat. Nanotechnol*. **2016**, *11*, 75-81.

(12) Yang, W.S.; Park, B.W.; Jung, E.H.; Jeon, N.J.; Kim, Y.C.; Lee, D.U.; Shin, S.S.; Seo, J.; Kim, E.K.; Noh, J.H.; Seok, SI. Iodide Management in Formamidinium-Lead-Halide–Based Perovskite Layers for Efficient Solar Cells. *Science* **2017**, *356*, 1376–1379.

(13) Leblanc, A.; Mercier, N.; Allain, M.; Dittmer, J.; Fernandez, V.; Pauporté, T. Lead and Iodide Deficient MAPI, d-MAPI: the Bridge Between 2D and 3D Hybrid Perovskites. *Angew. Chem., Int. Ed.*, **2017**, *56*, 16067 –16072

(14) Wang, P.; Ulfa, M.; Pauporté, T. Effects of Perovskite Monovalent Cation Composition on the High and Low Frequency Impedance Response of Efficient Solar Cells. *J. Phys. Chem. C* **2018**, *122* 1973−1981.

(15) Li, S.B.; Zhang, P.; Wang, Y.F.; Sarvari, H.; Liu, D.T.; Wu, J.; Yang, Y.J.; Wang, Z.M.; Chen, Z.D. Interface Engineering of High Efficiency Perovskite Solar Cells Based on ZnO Nanorods using Atomic Layer Deposition. *Nano Res*., **2017**, *10*, 1092-1103.

(16) Zhang, T.; Wu, J.; Zhang, P.; Ahmad, W.; Wang, Y.F.; Alqahtani, M.; Chen, H.; Gao, C.M.; Chen, Z.D.; Wang, Z.M.; Li, S.B. High Speed and Stable Solution-Processed Triple Cation Perovskite Photodetectors. *Adv. Optical Mater*. **2018**, *6*, 170134.

(17) Zhang, R.; Liu, D.T.; Wang, Y.F.; Zhang, T.; Gu, X.L.; Zhang, P.; Wu, J.; Chen, Z.D.; Zhao, Y.C.; Li, S.B. Theoretical Lifetime Extraction and Experimental Demonstration of Stable Cesium-Containing Tri-Cation Perovskite Solar Cells with High Efficiency. Electrochim. Acta, 2018, 265, 98-106.
(18) Wang, Y.; Wu, J.; Peng Zhang, P.; Liu, D.; Zhang, .T.; Ji, L.; Gu, X.; Chen, Z.D.; Li, S. Stitching Triple Cation Perovskite by a Mixed Anti-Solvent Process for High Performance Perovskite Solar Cells. *Nano Energy*, **2017**, *39*, 616–625

(19) Green, M.A.; Hishikawa, Y.; Dunlop, E.D.; Levi, D.H.; Hohl-Ebinger, J.; Ho-Baillie, A.W.Y. Solar Cell Efficiency Tables (version 52). *Prog. Photovoltaics*, **2018**, *26*, 427-436.

(20) Wang, P.; Shao, Z.; Ulfa, M.; Pauporté, T. Insights into the Hole Blocking Layer Effect on the Perovskite Solar Cell Performance and Impedance Response. *J. Phys. Chem. C*, **2017**, *121*, 9131–9141.

(21) Ulfa, M.; Pauporté, T.; Bui, T.T.; Goubard, F. Impact of Organic Hole Transporting Material and Doping on the Electrical Response of Perovskite Solar Cells. *J. Phys. Chem. C*. **2018**, *122*, 11651–11658.

(22) Ulfa, M.; Zhu, T.; Goubard, F.; Pauporté, T. Molecular versus Polymeric Hole Transporting Materials for Perovskite Solar Cell Application. *J. Mater. Chem. A*. **2018**, *6*, 13350-13358

(23) Song, J.X.; Zheng, E.Q.; Bian, J.; Wang, X.F.; Tian, W.J.; Sanehira, Y.; Miyasaka, T. Low-Temperature SnO_2-Based Electron Selective Contact for Efficient and Stable Perovskite Solar Cells. *J. Mater. Chem. A* **2015**, *3*, 10837-10844.

(24) Baena, J.P.C.; Steier, L.; Tress, W.; Saliba, M.; Neutzner, S.; Matsui, T.; Giordano, F.; Jacobsson, T.J.; Kandada, A.R.S.; Zakeeruddin, S.M.; Petrozza, A.; Abate, A.; Nazeeruddin, M.K.; Gratzel, M.; Hagfeldt, A. Highly Efficient Planar Perovskite Solar Cells Through Band Alignment Engineering. *Energy Environ. Sci*. **2015**, *8*, 2928-2934

(25) Jiang, Q.; Zhang, L.Q.; Wang, H.L.; Yang, X.L.; Meng, J.H.; Liu, H.; Yin, Z.G.; Wu, J.L.; Zhang, X.W.; You, J.B.; Enhanced Electron Extraction Using SnO_2 for High-Efficiency Planar-Structure $HC(NH_2)_2PbI_3$-Based Perovskite Solar Cells. *Nat. Energy* **2017**, *2*, 1-7.

(26) Xiong, L.B.; Qin, M.C.; Yang, G.; Guo, Y.X.; Lei, H.W.; Liu, Q.; Ke, W.J.; Tao H.; Qin, P.L.; Li, S.Z.; Yu, H.Q.; Fang, G.J. Performance Enhancement of High Temperature SnO_2-Based Planar Perovskite Solar Cells: Electrical Characterization and Understanding of the Mechanism. *J. Mater. Chem*. A **2016**, *4*, 8374-8383.

(27) Park, M.; Kim, J.Y.; Son, H.J.; Lee, C.H.; Jang, S.S.; Ko, M.J. Low-Temperature Solution-Processed Li-Doped SnO_2 as an Effective Electron Transporting Layer for High-Performance Flexible and Wearable Perovskite Solar Cells. *Nano Energy*, **2016**, *26*, 208-215.

(28) Chen, H.; Liu, D.T.; Wang, Y.F.; Wang, C.Y.; Zhang, T.; Zhang, P.; Sarvari, H.; Chen, Z.; Li, S.B. Enhanced Performance of Planar Perovskite Solar Cells Using Low-Temperature Solution-Processed Al-Doped SnO2 as Electron Transport Layers. *Nanoscale Res. Lett*. **2017**, *12*, 238.

(29) Yang, G.; Wang, C.L.; Lei, H.W.; Zheng, X.L.; Qin, P.L.; Xiong, L.B.; Zhao, X.Z.; Yan, Y.F.; Fang, G.J. Interface Engineering in Planar Perovskite Solar Cells: Energy Level Alignment, Perovskite Morphology Control and High Performance Achievement. *J. Mater. Chem. A* **2017**, *5*, 1658-1666.

(30) Ke, W.J.; Zhao, D.W.; Xiao, C.X.; Wang, C.L.; Cimaroli, A.J.; Grice, C.R.; Yang, M.J.; Li, Z.; Jiang, C.S.; Al-Jassim, M.; Zhu, K.; Kanatzidis, M.G.; Fang, G.J.; Yan, Y.F. Cooperative Tin Oxide

Fullerene Electron Selective Layers for High-Performance Planar Perovskite Solar Cells. *J. Mater. Chem. A* **2016**, *4*, 14276-14283.

(31) Anaraki, E.H.; Kermanpur, A.; Steier, L.; Domanski, K.; Matsui, T.; Tress, W.; Saliba, M.; Abate, A.; Gratzel, M.; Hagfeldt, A.; Correa-Baena, J.P. Highly Efficient and Stable Planar Perovskite Solar Cells by Solution-Processed Tin Oxide. *Energy Environ. Sci.* **2016**, *9*, 3128-3134.

(32) Chen, J.Y.; Chueh, C.C.; Zhu, Z.L.; Chen, W.C.; Jen, A.K.Y.Low-Temperature Electrodeposited Crystalline SnO_2 as an Efficient Electron Transporting Layer for Conventional Perovskite Solar Cells. *Sol. Energy Mater. Sol. Cells* **2017**, *164*, 47-55.

(33) Lin, S.Y.; Yang, B.C.; Qiu, X.C.; Yan, J.Q.; Shi, J.; Yuan, Y.B.; Tan, W.J.; Liu, X.L.; Huang, H.; Gao, Y.L.; Zhou, C.H. Efficient and Stable Planar Hole-Transport-Material-Free Perovskite Solar Cells Using Low Temperature Processed SnO_2 as Electron Transport Material. *Org. Electron.* **2018**, *53*, 235-241.

(34) Snaith, H.J.; Ducati, C. SnO_2-Based Dye-Sensitized Hybrid Solar Cells Exhibiting Near Unity Absorbed Photon-to-Electron Conversion Efficiency. *Nano Lett.* **2010**, *10*, 1259-1265.

(35) Dou, X.; Sabba, D.; Mathews, N.; Wong, L. H.; Lam, Y. M.; Mhaisalkar, S. Hydrothermal Synthesis of High Electron Mobility Zn doped SnO_2 Nanoflowers as Photoanode Material for Efficient Dye Sensitized Solar Cells. *Chem. Mater.* **2011**, *23*, 3938−3945.

(36) Arnold, M. S.; Avouris, P.; Pan, Z. W.; Wang, Z. L. Field-effect Transistors Based on Single Semiconducting Oxide Nanobelts. *J. Phys. Chem. B* **2003**, *107*, 659−663.

(37) Guerrero, A.; Garcia-Belmonte, G.; Mora-Sero, I.; Bisquert, J.; Kang, Y.S.; Jacobsson, T.J.; Correa-Baena, J.P.; Hagfeldt, A. Properties of Contact and Bulk Impedances in Hybrid Lead Halide Perovskite Solar Cells Including Inductive Loop Elements. *J. Phys. Chem. C* **2016**, *120*, 8023−8032.

(38) Ahn, N.; Son, D.Y.; Jang, I.H.; Kang, S.M.; Choi, M.; Park, N.G. Highly Reproducible Perovskite Solar Cells with Average Efficiency of 18.3% and Best Efficiency of 19.7% Fabricated via Lewis Base Adduct of Lead(II) Iodide. *J. Am. Chem. Soc.* **2015**, *137*, 8696-8699.

(39) Ke, W.J.; Zhao, D.W.; Xiao, C.X.; Wang, C.L.; Cimaroli, A.J.; Grice, C.R.; Yang, M.J.; Li, Z.; Jiang, C.S.; Al-Jassim, M.; Zhu, K.; Kanatzidis, M.G.; Fang, G.J.; Yan, Y.F. Cooperative Tin Oxide Fullerene Electron Selective Layers for High-Performance Planar Perovskite Solar Cells. *J. Mater. Chem. A* **2016**, *4*, 14276−14283

(40) Guérin, V.M.; Elias, J.; Nguyen, T.T.; Philippe, L.; Pauporté, T., Ordered Networks of ZnO-Nanowire Hierarchical Urchin-Like Structures for Improved Dye-Sensitized Solar Cells. *Phys. Chem. Chem. Phys.* **2012**, *14*, 12948-12955.

(41) Magne, C.; Dufour, F.; Labat, F.; Lancel, G.; Durupthy, O. ; Cassaignon, S.; Pauporté, T. Effects of TiO_2 Nanoparticle Polymorphism on Dye-Sensitized Solar Cell Photovoltaic Properties. *J. Photochem. Photobiol., A* **2012**, *232*, 22-31.

(42) Pitarch-Tena, D.; Ngo, T.T.; Vallés-Pelarda, M.; Pauporté, T.; Mora-Seró, I. Impedance Spectroscopy Measurements in Perovskite Solar Cells. Device Stability During the Measurement and Noise Reduction. *ACS Energy Lett.*, **2018**, *3*, 1044−1048.

(43) Shi, D.; Adinolfi, V.; Comin, R.; Yuan, M.; Alarousu, E.; Buin, A.; Chen, Y.; Hoogland, S.; Rothenberger, A.; Katsiev, K. Low Trap-State Density and Long Carrier Diffusion in Organolead Trihalide Perovskite Single Crystals. *Science*. **2015**, *347*, 519-22.

(44) Staub, F.; Hempel, H.; Hebig, J.C.; Mock, J.; Paetzold, U.W.; Rau, U.; Unold, T.; Kirchartz, T. Beyond Bulk Lifetimes: Insights into Lead Halide Perovskite Films from Time-Resolved Photoluminescence. *Phys. Rev. Appl.* **2016**, *6*, 044017.

(45) Pascoe A.R; Duffy, N.W.; Scully, A.D.; Huang, F.; Cheng, Y.B. Insights into Planar $CH_3NH_3PbI_3$ Perovskite Solar Cells using Impedance Spectroscopy. *J. Phys. Chem. C* **2015**, *119*, 4444−4453

(46) Juarez-Perez, E.J.; Wuβler, M.; Fabregat-Santiago, F.; Lakus-Wollny,K.; Mankel, E.; Mayer, T.; Jaegermann, W.; Mora-Sero, I. Role of the Selective Contacts in the Performance of Lead Halide Perovskite Solar Cells. *J. Phys. Chem. Lett.* **2014**, *5*, 680−685.

(47) Juarez-Perez, E.J.; Sanchez, R.S.; Badia, L.; Garcia-Belmonte, G.; Kang, Y.S.; Mora-Sero, I.; Bisquert, J. Photoinduced Giant Dielectric Constant in Lead Halide Perovskite Solar Cells. *J. Phys. Chem. Lett*. **2014**, *5*, 2390−2394.

(48) Dualeh, A.; Moehl, T.; Tétreault, N.; Teuscher, J.; Gao, P.; Nazeeruddin, M.K.; Grätzel, M. Impedance Spectroscopic Analysis of Lead Iodide Perovskite-Sensitized Solid-State Solar Cells. *Sci. Rep*. **2014**, *8*, 362–373.

(49) Gonzalez-Pedro, V.; Juarez-Perez, E.J.; Arsyad, W.S.; Barea, E.M.; Fabregat-Santiago, F.; Mora-Sero, I.; Bisquert, J. General Working Principles of $CH_3NH_3PbX_3$ Perovskite Solar Cells. *Nano Lett.* **2014**, *14*, 888−893.

(50) Almora, O.; Zarazua, I.; Mas-Marza, E.; Mora-Sero, I.; Bisquert, J.; Garcia-Belmonte, G. Capacitive Dark Currents, Hysteresis, and Electrode Polarization in Lead Halide Perovskite Solar Cells. *J. Phys. Chem. Lett.* **2015**, *6*, 1645−1652.

(51) Guerrero, A.; Juarez-Perez, E. J.; Bisquert, J.; Mora-Sero, I.; Garcia-Belmonte, G. Electrical Field Profile and Doping in Planar Lead Halide Perovskite Solar Cells. *Appl. Phys. Lett*. **2014**, *105*, 133902.

(52) Almora, O.; Guerrero, A.; Garcia-Belmonte, G. Ionic Charging by Local Imbalance at Interfaces in Hybrid Lead Halide Perovskites. *Appl. Phys. Lett*. **2016**, *108*, 043903.

(53) Kim, H.-S.; Mora-Sero, I.; Gonzalez-Pedro, V.; Fabregat-Santiago, F.; Juarez-Perez, E. J.; Park, N.-G.; Bisquert, J. Mechanism of Carrier Accumulation in Perovskite Thin-Absorber Solar Cells. *Nat. Commun*. **2013**, *4*, 2242.

(54) Zarazua, I.; Han, G.F.; Boix, P.P.; Mhaisalkar, S.; Fabregat-Santiago, F.; Mora-Sero, I.; Bisquert, J.; Garcia-Belmonte, G. Surface Recombination and Collection Efficiency in Perovskite Solar Cells from Impedance Analysis. *J. Phys. Chem. Lett*., **2016**, *7*, 5105-5113.

(55) Yang, T.-Y.; Gregori, G.; Pellet, N.; Grätzel, M.; Maier, J. The Significance of Ion Conduction in a Hybrid Organic-Inorganic Lead Iodide-Based Perovskite Photosensitizer. *Angew. Chem., Int. Ed.* **2015**, *54*, 7905−7910.

(56) Kim, H.-S.; Jang, I.-H.; Ahn, N.; Choi, M.; Guerrero, A.; Bisquert, J.; Park, N.-G. Control of I-V Hysteresis in $CH_3NH_3PbI_3$ Perovskite Solar Cell. *J. Phys. Chem. Lett*. **2015**, *6*, 4633−4639.

Please cite this paper as : M. Ulfa, P. Wang, J. Zhang, J. Liu, W. Daney de Marcillac, L. Coolen, S. Peralta, T. Pauporté, Charge Injection and Electrical Response in Low Temperature SnO2-Based Efficient Perovskite Solar Cells. ACS Appl. Mater. Interfaces, 10 (2018) 35118–35128.

(57) Anaya M.; Zhang, W.; Clasen Hames, B.; Li, Y.; Fabregat-Santiago, F.. Calvo, M.E.; Snaith, H.J.; Miguez, H.; Mora-Sero I. Electron Injection and Scaffold Effects in Perovskite Solar Cells. *J. Mater. Chem. C* **2017**, *5*, 634-644

Please cite this paper as : M. Ulfa, P. Wang, J. Zhang, J. Liu, W. Daney de Marcillac, L. Coolen, S. Peralta, T. Pauporté, Charge Injection and Electrical Response in Low Temperature SnO2-Based Efficient Perovskite Solar Cells. ACS Appl. Mater. Interfaces, 10 (2018) 35118–35128.

TOC Graphic